

Learning by Aligning 2D Skeleton Sequences in Time

Quoc-Huy Tran*

Muhammad Ahmed*
Andrey Konin

M. Hassan Ahmed
M. Zeeshan Zia

Murad Popattia

Retrocausal, Inc.
Redmond, WA
www.retrocausal.ai

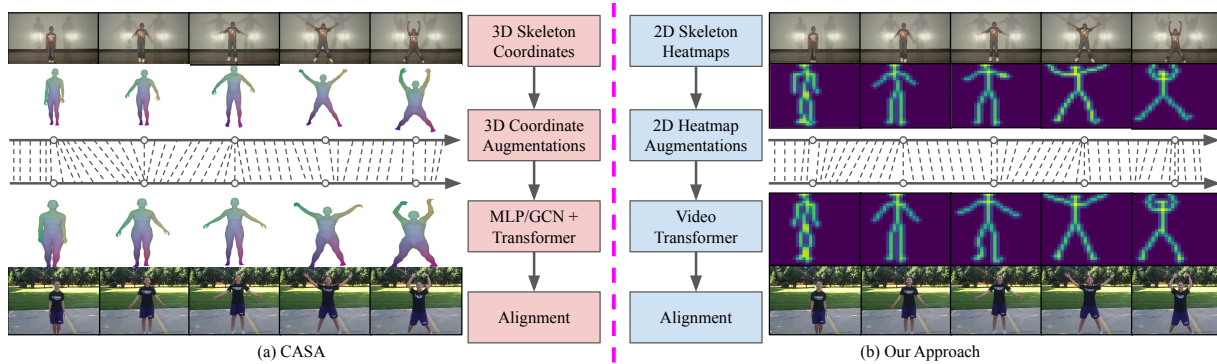


Figure 1. (a) The state-of-the-art method in video-based self-supervised learning, i.e., CASA, uses 3D skeleton-based temporal video alignment as a pretext task and performs 3D skeleton augmentations. (b) Our approach relies on 2D skeleton-based temporal video alignment and conducts 2D skeleton augmentations. We use 2D skeleton heatmaps, which are fed to a video transformer for learning useful spatiotemporal and contextual features. Our method obtains higher accuracy and better robustness against missing and noisy keypoints, while showing superior performance in various fine-grained human activity understanding tasks. Moreover, using both 2D skeleton heatmaps and RGB videos as inputs establishes the state-of-the-art across all metrics and datasets.

Abstract

This paper presents a self-supervised temporal video alignment framework which is useful for several fine-grained human activity understanding applications. In contrast with the state-of-the-art method of CASA, where sequences of 3D skeleton coordinates are taken directly as input, our key idea is to use sequences of 2D skeleton heatmaps as input. Unlike CASA which performs self-attention in the temporal domain only, we feed 2D skeleton heatmaps to a video transformer which performs self-attention both in the spatial and temporal domains for extracting effective spatiotemporal and contextual features. In addition, we introduce simple heatmap augmentation techniques based on 2D skeletons for self-supervised learning. Despite the lack of 3D information, our approach achieves not only higher accuracy but also better robustness against missing and noisy keypoints than CASA. Furthermore, extensive evaluations on three public datasets, i.e., Penn Ac-

tion, IKEA ASM, and H2O, demonstrate that our approach outperforms previous methods in different fine-grained human activity understanding tasks. Finally, fusing 2D skeleton heatmaps with RGB videos yields the state-of-the-art on all metrics and datasets. To the best of our knowledge, our work is the first to utilize 2D skeleton heatmap inputs and the first to explore multi-modality fusion for temporal video alignment.

1. Introduction

We investigate the problem of temporal video alignment [22,30,41,49,59], which aims to find dense framewise correspondences between two videos capturing the same activity, despite discrepancies in human appearance, background clutter, human motion, and camera viewpoint. To obtain perfect temporal alignments, methods must be able to recognize not only the action phases but also their causal

relationships. Temporal video alignment plays an important role in many fine-grained human activity understanding applications, including anomaly detection [22] (i.e., detect deviations from a dataset of normal videos) and skill transfer [41] (i.e., provide feedback to learners based on a dataset of expert demonstration videos).

We are interested in self-supervised approaches for temporal video alignment, since acquiring fine-grained correspondence labels is generally hard and costly. Early methods [22, 30, 49, 59] attempt to match video frames directly. They optimize temporal alignment metrics such as dynamic time warping [17] and optimal transport [16] for self-supervised learning. Although the learned representations show promising generalization to downstream tasks, the results are far from being practical. Recently, CASA [41] proposes a context-aware self-supervised method for temporal video alignment, which operates on 3D skeletons (see Fig. 1(a)). It conducts 3D skeleton-based augmentations for self-supervised learning, while employing a transformer [69] to learn contextual features, yielding great results. Since CASA [41] directly processes 3D skeleton coordinates, its performance is greatly affected by human pose estimation errors such as noisy and missing keypoints.

In this paper, we present a self-supervised temporal video alignment method, which relies on 2D skeletons (see Fig. 1(b)). Motivated by the strong performance of [21] in skeleton-based action recognition, we first convert sequences of 2D skeletons into sequences of heatmaps, where each joint is modeled as a Gaussian distribution, making it less sensitive to human pose estimation errors. Unlike CASA [41] which performs self-attention in the temporal domain only, we pass the heatmap sequences to our alignment network, which adopts a video transformer [2] to perform self-attention both in the spatial and temporal domains, yielding effective spatiotemporal and contextual features. Moreover, we propose simple various heatmap augmentation strategies based on 2D skeletons for self-supervised learning. As compared to CASA [41], our method based on 2D skeleton heatmaps obtains both higher accuracy and better robustness against missing and noisy keypoints despite lacking 3D information. Moreover, we show superior performance of our approach over previous methods in fine-grained human activity understanding tasks on three public datasets. Lastly, utilizing both 2D skeleton heatmaps and RGB videos as inputs achieves the state-of-the-art across all metrics and datasets.

In summary, our contributions include:

- We propose a novel 2D skeleton-based self-supervised temporal video alignment approach with applications in fine-grained human activity understanding. We utilize 2D skeleton heatmaps as input and a video transformer for learning useful spatiotemporal and contextual features from 2D skeleton heatmaps. For self-

supervised learning, we introduce different 2D skeleton heatmap augmentation techniques.

- Our 2D skeleton-based approach is more accurate and robust against noisy and missing keypoints than CASA [41] which requires 3D skeletons. Our experiments on Penn Action, IKEA ASM, and H2O datasets show that our approach outperforms previous methods on several fine-grained human activity understanding tasks. Our multi-modality version achieves the state-of-the-art on all metrics and datasets.
- To our best knowledge, our work is the first to exploit 2D skeleton heatmap inputs and the first to perform multi-modality fusion for temporal video alignment.

2. Related Work

Self-Supervised Learning. Considerable efforts have been made in developing pretext tasks with pseudo labels for training image-based self-supervised models. A few examples include image colorization [42, 43], object counting [50, 55], predicting rotations [25], solving puzzles [8, 37], image inpainting [34], and image clustering [9, 10]. Recently, several works [11–13, 28] focus on designing data augmentation and contrastive learning strategies, which are important for learning effective image-based self-supervised representations. Unlike the above image-based methods, video-based methods, which exploit both spatial cues and temporal cues in videos, have attracted a great amount of interests recently. They learn video-based self-supervised representations by using pretext tasks such as future frame prediction [1, 20, 63, 70] and frame clustering [39], or leveraging temporal information such as temporal coherence [27, 54, 80], temporal order [24, 44, 52, 73], arrow of time [57, 72], and pace [5, 71, 76], or utilizing contrastive learning techniques [19, 23, 33, 58].

More recently, skeleton-based methods, which operate on skeleton data, have been introduced. They learn skeleton-based self-supervised representations by using pretext tasks such as skeleton inpainting [78] and motion prediction [64], or utilizing neighborhood consistency [60], motion continuity [65], and multiple pretext tasks [46]. The above methods often do not exploit spatiotemporal dependencies. In this work, we use 2D skeleton-based alignment as a pretext task and 2D skeleton-based augmentation for self-supervised learning. Our approach exploits dependencies between joints in the same skeleton as well as between skeletons in the same sequence and across the sequences.

Temporal Video Alignment. Despite significant progress in unsupervised time series alignment, methods for self-supervised temporal video alignment have been developed only recently. To learn self-supervised representations, TCN [59] employs contrastive learning on synchronized

frames across viewpoints, while TCC [22] imposes cycle-consistent frame correspondences across videos. Recently, LAV [30] and VAVA [49] adopt dynamic time warping [17] and optimal transport [16] respectively as temporal video alignment losses. The above methods focus on aligning video frames directly. More recently, CASA [41] presents a self-supervised temporal video alignment method which operates on 3D skeletons. In this paper, we propose a 2D skeleton-based self-supervised temporal video alignment method, which is more accurate and robust against noisy and missing keypoints despite lacking 3D information.

Skeleton-Based Action Recognition. There exist notable interests in skeleton-based action recognition due to its compactness. A popular group of methods [7, 14, 29, 61, 62, 75] model the skeleton sequence as a spatiotemporal graph and rely on Graph Convolutional Networks (GCNs). Despite great results, their drawbacks lie in robustness to noisy/incomplete skeletons [79], scalability with multi-person actions, and fusion with other modalities [18]. Another group of methods convert the skeleton sequence into a 2D input (e.g., heatmap aggregation [3, 15, 74] and coordinate aggregation [6, 36, 45, 51]) or a 3D input (e.g., stacked pseudo images [32, 47] and cuboid [48]) and employ Convolutional Neural Networks (CNNs). These methods often suffer from information loss during aggregation, yielding inferior results. To address that, Duan et al. [21] convert each skeleton into a heatmap and pass the heatmap sequence, which preserves all information, to a CNN. Their method achieves superior results while alleviating the above issues of GCN-based methods. Inspired by their method, we propose a self-supervised temporal video alignment framework for fine-grained human activity understanding.

3. Our Approach

Below we describe our main contribution, a video-based self-supervised learning method using 2D skeleton-based temporal video alignment as a pretext task. An overview of our approach is illustrated in Fig. 2.

Notations. Let us denote $\mathbf{S} = \{s_1, s_2, \dots, s_M\}$ and $\mathbf{S}' = \{s'_1, s'_2, \dots, s'_N\}$ as the original 2D skeleton sequence and its augmented sequence, with length M and N respectively. Each 2D skeleton has K 2D joints, i.e., $s_i \in \mathbb{R}^{K \times 2}$ and $s'_j \in \mathbb{R}^{K \times 2}$. The heatmaps obtained from \mathbf{S} and \mathbf{S}' are written as $\mathbf{H} = \{h_1, h_2, \dots, h_M\}$ and $\mathbf{H}' = \{h'_1, h'_2, \dots, h'_N\}$, with h_i and h'_j computed from s_i and s'_j respectively. Next, let us represent the embedding function (up to the cross attention module) as f_θ , with learnable parameters θ . The embedding features of \mathbf{H} and \mathbf{H}' are expressed as $\mathbf{U} = \{u_1, u_2, \dots, u_M\}$ and $\mathbf{U}' = \{u'_1, u'_2, \dots, u'_N\}$, with $u_i = f_\theta(h_i)$ and $u'_j = f_\theta(h'_j)$ respectively. Lastly, we denote the projection head function as g_ϕ , with learnable parameters ϕ . The latent features before the loss function are written as

$\mathbf{Z} = \{z_1, z_2, \dots, z_M\}$ and $\mathbf{Z}' = \{z'_1, z'_2, \dots, z'_N\}$, with $z_i = g_\phi(u_i)$ and $z'_j = g_\phi(u'_j)$ respectively.

3.1. 2D Skeleton Heatmap

Here we discuss the estimation of 2D skeletons \mathbf{S} and their corresponding heatmaps \mathbf{H} from a video sequence. Unlike CASA [41], which requires 3D skeletons, our method is based on 2D skeletons. In general, due to the additional depth estimation task, obtaining accurate 3D skeletons is more difficult than obtaining accurate 2D skeletons. As suggested in [21], we can use a state-of-the-art human detector and top-down 2D human pose estimator such as Faster-RCNN [26] and HRNet [67] to obtain good quality 2D skeletons. For memory efficiency, a 2D skeleton is often stored as a set of 2D joint triplets $\{(x_k, y_k, c_k)\}$, where (x_k, y_k) are the 2D coordinates and c_k is the (maximum) confidence score of the k -th joint. In practice, for a fair comparison, we use the 2D skeletons that are projected from the 3D skeletons provided by CASA [41] and set $c_k = 1.0$.

We now convert 2D skeletons into heatmaps. For a 2D skeleton, we compute a heatmap of size $K \times H \times W$, where K is the number of 2D joints, and H and W are the height and width of the video frame respectively. Given a set of 2D joint triplets $\{(x_k, y_k, c_k)\}$, a *joint* heatmap h^J consisting of K Gaussian maps centered at every joint is derived as:

$$h_{kij}^J = e^{-\frac{(i-x_k)^2 + (j-y_k)^2}{2\sigma^2}} * c_k, \quad (1)$$

where σ is the standard deviation parameter of the Gaussian maps. Similarly, a *limb* heatmap h^L of size $L \times H \times W$ (L is the number of limbs in a skeleton) is written as:

$$h_{lij}^L = e^{-\frac{\text{dist}((i,j), \text{seg}(a_l, b_l))}{2\sigma^2}} * \min(c_{a_l}, c_{b_l}), \quad (2)$$

where the l -th limb is the segment $\text{seg}(a_l, b_l)$ between the two joints a_l and b_l , and the dist function computes the distance from the location (i, j) to the segment $\text{seg}(a_l, b_l)$. As we will show later in Sec. 4.1.2, combining both joint and limb heatmaps as input to our alignment network yields the best results, i.e., for each 2D skeleton s_i , we extract the combined heatmap $h_i = h_i^{J+L}$. Moreover, since the action of interest appears only in a small region in the video frames, we crop the heatmaps along the spatial dimensions using the smallest bounding box containing all 2D skeletons in the video sequence and resize them to the spatial dimensions of 30×30 . Thus, we reduce the size of the heatmaps, while preserving all 2D skeletons and their motions.

3.2. 2D Skeleton Heatmap Augmentation

Below we describe our simple heatmap augmentation techniques based on 2D skeletons, which are used to generate correspondence labels for self-supervised training of our alignment network. This is in contrast with the coordinate

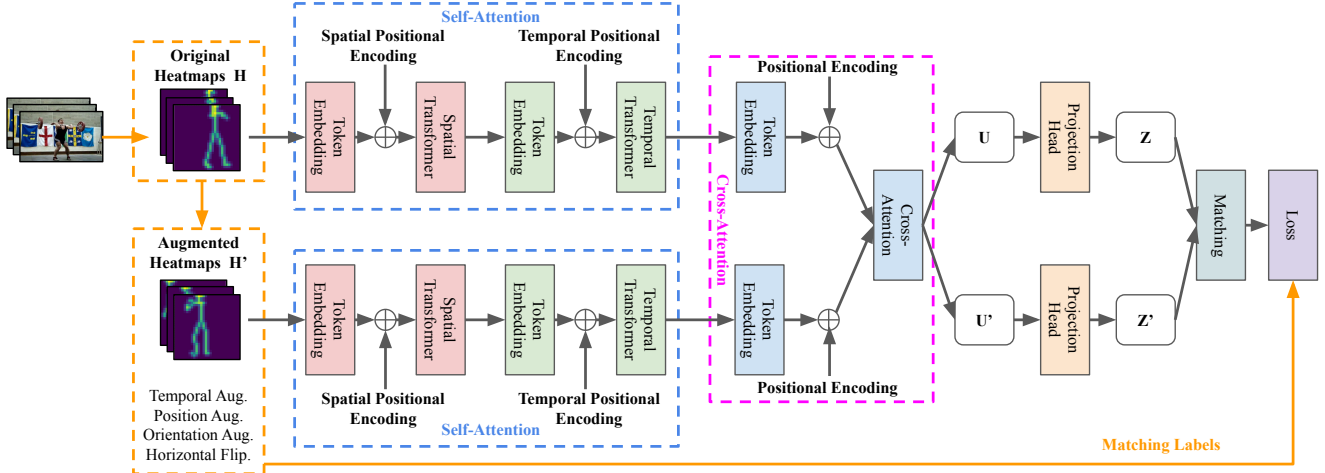


Figure 2. During training, our approach takes as input sequences of original heatmaps and augmented heatmaps. We perform self-attention (via spatial and temporal transformers with spatial and temporal positional encodings respectively) to extract effective spatiotemporal and contextual cues within each sequence and cross-attention to extract contextual cues across the sequences. The extracted features (after projection heads) are passed to a matching module which uses a contrastive regression formulation to predict correspondences across the sequences. Matching labels generated by the augmentation module are used in the loss function for self-supervised learning.

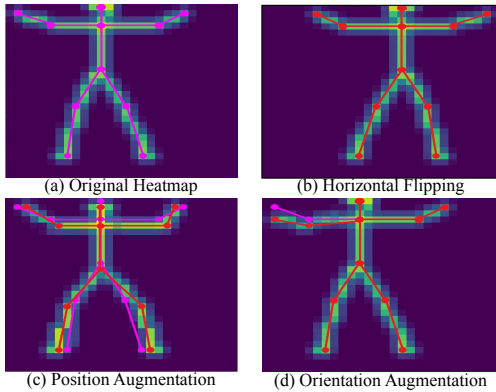


Figure 3. Examples of our heatmap augmentation techniques based on 2D skeletons. The original 2D skeleton is in pink, while the augmented 2D skeleton is in red.

augmentation techniques in CASA [41], which rely on 3D skeletons. We first apply various augmentations on the original 2D skeletons \mathcal{S} to obtain the augmented 2D skeletons \mathcal{S}' , and then compute the augmented heatmaps \mathbf{H}' from the augmented 2D skeletons \mathcal{S}' . Our augmentations include: temporal augmentation, position augmentation, orientation augmentation, and horizontal flipping.

Temporal Augmentation. We adjust the action speed by randomly selecting N 2D skeletons out of the M 2D skeletons in \mathcal{S} , resulting in \mathcal{S}' .

Position Augmentation. We perturb the 2D joints in \mathcal{S} by adding a random noise (sampled from a Gaussian distribution $\mathcal{N}(\nu)$ with a standard deviation ν), yielding \mathcal{S}' .

Orientation Augmentation. We pick a limb in \mathcal{S} (e.g., arm, leg) and rotate it by a random angle (sampled from a Gaussian distribution $\mathcal{N}(\rho)$ with a standard deviation ρ), resulting in \mathcal{S}' .

Horizontal Flipping. We flip the 2D joints in \mathcal{S} from left to right and vice versa, yielding \mathcal{S}' .

Fig. 3 shows examples of our simple heatmap augmentation techniques based on 2D skeletons. For position and orientation augmentations, we empirically use a multivariate Gaussian distribution with a covariance matrix so that the added noise is temporally smooth as in CASA [41]. However, it does not lead to improved results and is thus not used in the above. Furthermore, the above augmentations generate correspondence labels between \mathcal{S} and \mathcal{S}' (and similarly, between \mathbf{H} and \mathbf{H}'), which can be used for self-supervised training of our alignment network in the next section.

3.3. 2D Skeleton-Based Self-Supervised Temporal Video Alignment

Below we describe our network architecture and loss: **Self-Attention.** Given the original heatmap sequence \mathbf{H} and the augmented sequence \mathbf{H}' , we pass them separately through a video transformer, namely ViViT [2], to perform self-attention both in the spatial and temporal domains, yielding effective spatiotemporal and contextual cues within each sequence. Below we discuss the processing of \mathbf{H} only since the same is applied for \mathbf{H}' . For each \mathbf{h}_i in \mathbf{H} , we first break it into $h * w$ non-overlapping patches, which are embedded via linear projection into $h * w$ tokens. The tokens from \mathbf{h}_i (with spatial positional encoding) are then fed to a spatial transformer, which learns in-

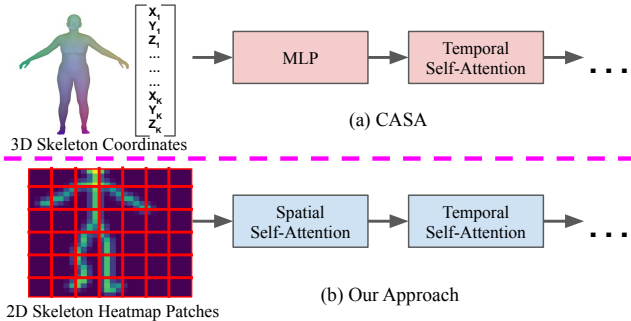


Figure 4. (a) CASA directly processes 3D skeleton coordinates and conducts self-attention in the temporal domain only. (b) Our approach operates on 2D skeleton heatmaps and performs self-attention both in the spatial and temporal domains.

teractions between tokens from the same temporal index (i.e., between joints in the same skeleton). Next, we employ global average pooling on the above tokens output by the spatial transformer to obtain the frame-level token representing h_i . The frame-level tokens of H (with temporal positional encoding) are passed together to a temporal transformer, which learns interactions between tokens from different temporal indexes (i.e., between skeletons in the same sequence). Note that our approach performs self-attention both in the spatial and temporal domains, whereas CASA [41] conducts self-attention in the temporal domain only. Fig. 4 illustrates this difference. In addition, our positional encodings are learned, whereas the positional encoding in CASA [41] is fixed.

Cross-Attention. The above modules only focus on self-attention in the spatial and temporal domains within each sequence. Following [41,66], we add a cross-attention module to learn interactions between H and H' (i.e., between skeletons across the sequences), yielding contextual cues across the sequences. In particular, we encode the tokens output by the self-attention modules via an MLP layer and positional encoding before applying cross-attention.

Projection Head. We include a projection head, which is an MLP network with one hidden layer. As mentioned in [12,41], adding the projection head improves the generalization ability and yields effective features for downstream fine-grained human activity understanding tasks.

Matching and Loss. We first compute the probability ω_{ij} that the i -th frame in H is matched with the j -th frame in H' using contrastive regression [22,41] as:

$$\omega_{ij} = \frac{e^{-\|z_i - z'_j\|/\lambda}}{\sum_{m=1}^M e^{-\|z_m - z'_j\|/\lambda}}, \quad (3)$$

where λ is a temperature parameter. The above formulation encourages temporally close frames to be mapped to nearby points and temporally distant frames to be mapped to far away points in the latent space. The frame index i_j^{pred} in H

corresponding to the j -th frame in H' is then predicted as $i_j^{pred} = \sum_{i=1}^M i * \omega_{ij}$. The matching labels between H and H' are obtained in the augmentation module and hence can be used as supervision signals for training our alignment network. The difference between the predicted frame index i_j^{pred} and ground truth frame index i_j^{gt} is minimized as:

$$\mathcal{L} = \frac{1}{N} \sum_{j=1}^N \|i_j^{pred} - i_j^{gt}\|^2. \quad (4)$$

4. Experiments

Datasets. We evaluate our approach on IKEA ASM [4], H2O [40], and Penn Action [77]. Following [30,41,49], we experiment on the *Kallax Drawer Shelf* videos of IKEA ASM [4], which demonstrates furniture assembly activities. H2O [40] is a hand-object interaction dataset with left and right hand poses, object poses, and interaction labels. We evaluate on the *Pouring Milk* activity as [41]. Penn Action [77] contains various sporting activities. For evaluation, we utilize the same subset of 13 actions as [22,30,41,49]. We use full-body poses as our input for Penn Action [77] and IKEA ASM [4], hand poses as our input for H2O [40], and the same training and testing splits for all datasets as [22,30,41,49].

Implementation Details. Our approach is implemented in pyTorch [56]. We randomly initialize our model and use ADAM [38] optimization. We reduce the learning rate by a ratio of 0.5 at each of the 24 epochs. For Penn Action [77], one model is trained separately for each of the 13 actions. For datasets with a single action such as IKEA ASM [4] and H2O [40], a single model is trained. Due to space limits, more details are available in the supplementary material.

Competing Methods. We test our approach, namely LA2DS (short for *Learning by Aligning 2D Skeletons*), against state-of-the-art self-supervised temporal video alignment methods, including SAL [53], TCN [59], TCC [22], LAV [30], VAVA [49], and CASA [41]. Moreover, we combine CASA [41] with the graph convolutional network STGCN [75], and integrate LAV [30] with the video transformer ViViT [2] (pre-trained on Kinetics-400 [35]) as additional competing methods.

Evaluation Metrics. We compute four metrics on the validation set. We train the network on the training set and freeze it, and then train an SVM classifier or a linear regressor on top of the frozen features. We use the below metrics:

- *Phase Classification Accuracy* is defined as the percentage of correctly classified frames for fine-grained action recognition, achieved by training an SVM classifier on extracted features to predict phase labels.
- *Phase Progression* measures the ability of the learned representations to predict the progress of an action over

	Method	Class.	Progress.	τ
H2O	w/o Temp. Transf.	64.40	0.9149	0.9566
	w/o Proj. Head	66.53	0.9169	0.9590
	w/o Pos. Enc.	67.80	0.9196	<u>0.9615</u>
	w/o Cross Attent.	67.83	<u>0.9198</u>	0.9590
	w/o Spat. Transf.	<u>68.47</u>	0.9039	0.9548
	All	70.12	0.9280	0.9670

Table 1. Effects of different model components. Best results are in **bold**, while second best ones are underlined.

time, computed as the average R-squared measure between the ground truth progress values and those predicted by a linear regressor trained on the embeddings.

- *Kendall’s Tau* is used to assess the temporal alignment of two sequences. It is in $[-1,1]$, where 1 denotes perfect alignment and -1 denotes alignment in reverse order. This metric does not require any labels and assumes a strictly monotonic order of actions.
- *Average Precision* measures the accuracy of fine-grained frame retrieval, calculated as the proportion of retrieved frames with the same phase labels as the query frame. It ranges in $[0,1]$, where a value close to 1 denotes great performance and vice versa.

4.1. Ablation Results

In the following, we perform ablation experiments on the H2O dataset to evaluate the effectiveness of our design choices in Sec. 3. Moreover, we study the robustness of our approach in the presence of missing and noisy keypoints.

4.1.1 Effects of Different Model Components

The ablation results of various network components in Tab. 1 demonstrate that all of our network components in Sec. 3.3 consistently enhance the performance, and removing any of them leads to a performance drop. Specifically, removing spatial and temporal transformers causes a performance decline because self-attention captures spatiotemporal and contextual cues within a sequence. Importantly, removing spatial transformer yields the worst results on both phase progression and Kendall’s Tau. Cross-attention is crucial for extracting context across sequences, while positional encoding provides location information. The benefit of non-linear transformations is highlighted by a performance decrease when the projection head is removed.

4.1.2 Effects of Different Heatmaps

We now conduct an ablation study on the H2O dataset by using various heatmaps in Sec. 3.1 as input to our network,

	Method	Class.	Progress.	τ
H2O	Limbs	<u>67.72</u>	0.9099	0.9614
	Joints	66.09	<u>0.9101</u>	<u>0.9646</u>
	Limbs+Joints	70.12	0.9280	0.9670

Table 2. Effects of different heatmaps. Best results are in **bold**, while second best ones are underlined.

	Method	Input	Keypoint Missing Probability p			
			0%	25%	50%	100%
H2O	CASA [41]	▲	68.78	66.68	64.80	60.93
	LA2DS (Ours)	★	70.12	69.54	69.02	68.94

Table 3. Robustness against missing keypoints. Note that ▲ denotes 3D pose coordinate inputs, while ★ denotes 2D pose heatmap inputs. Best results are in **bold**.

including joint heatmaps only, limb heatmaps only, and combined joint+limb heatmaps. Tab. 2 illustrates the results of this ablation study. It is evident from Tab. 2 that using integrated joint+limb heatmaps as input to our network leads to the best results, outperforming using joint heatmaps or limb heatmaps alone.

4.1.3 Robustness against Missing Keypoints

To assess the robustness of our method, we perform an experiment where a certain part of the skeleton is removed. Specifically, we randomly remove one finger with a probability p for each frame in the H2O dataset during testing (without any finetuning) and measure the impact of this perturbation on the performance of classification accuracy. The results in Tab. 3 show that LA2DS exhibits a high level of robustness to missing keypoints. For example, when one finger is dropped per frame (i.e., $p = 100\%$), the decrease in accuracy for LA2DS is minimal (about 1%), whereas for CASA [41], the drop in accuracy is around 8%. This is likely because our method represents each joint by a Gaussian distribution and performs self-attention in the spatial domain to leverage dependencies between joints in the same skeleton, whereas CASA [41] models each joint merely by its coordinates and does not conduct self-attention in the spatial domain.

4.1.4 Robustness against Noisy Keypoints

To examine the generalization of our approach to noisy keypoints, we train and test on skeletons of different qualities. In particular, we use ground truth keypoints provided by the H2O dataset, namely *clean* keypoints, as well as add random noise to them, yielding *noisy* keypoints. We measure the impact of this perturbation on the performance via clas-

	Method	Input	Train Data \Rightarrow Test Data			
			C \Rightarrow C	C \Rightarrow N	N \Rightarrow C	N \Rightarrow N
H2O	CASA [41]	▲	68.78	65.15	65.09	63.69
	LA2DS (Ours)	★	70.12	68.59	68.75	68.23

Table 4. Robustness against noisy keypoints. Note that ▲ denotes 3D pose coordinate inputs, while ★ denotes 2D pose heatmap inputs. C denotes clean (ground truth) keypoints, while N denotes noisy keypoints. Best results are in **bold**.

sification accuracy. The results are reported in Tab. 4. It is clear from Tab. 4 that LA2DS exhibits a high level of robustness against noisy keypoints. For instance, when noisy keypoints are used for both training and testing, the accuracy of CASA [41] is decreased by more than 5%, whereas our method has an accuracy drop of less than 2%. Similar to the prior section, our method is more robust to noisy keypoints than CASA [41], thanks to our heatmap representation and self-attention in the spatial domain.

4.2. Comparisons with the State-of-the-Art

Below we quantitatively compare our approach with previous methods in various fine-grained human activity understanding tasks on three public datasets. Also, qualitative comparisons are provided in the supplementary material.

4.2.1 Phase Classification Results

We first evaluate the effectiveness of our learned representations for action phase classification. Tab. 5 reports the quantitative results of all methods on Penn Action, IKEA ASM, and H2O. It is evident from Tab. 5 that our method achieves the best overall performance. The inferior performance of ViViT [2]+LAV [30] is likely because ViViT [2] has roughly one fifth number of parameters of ResNet-50 [31] used in the original LAV [30]. In contrast, we empirically observe that STGCN [75]+CASA [41] often suffers from overfitting due to low-dimensional input vectors. The results in Tab. 5 indicate that LA2DS is effective in learning spatiotemporal and contextual features, yielding superior classification performance.

4.2.2 Phase Progression and Kendall’s Tau Results

Tab. 6 presents the phase progression and Kendall’s Tau results on Penn Action and H2O (IKEA ASM is not included due to its repetitive labels [30]). Phase progression measures how well an action progresses over the video, whereas Kendall’s Tau measures how well two sequences are aligned temporally. From Tab. 6, it can be seen that our approach obtains the best performance in Kendall’s Tau, while having comparably best numbers along with CASA [41] in

	Method	Input	Amount of Labels		
			10%	50%	100%
Penn Action	SAL [53]	□	79.94	81.11	81.79
	TCN [59]	□	81.99	82.64	82.78
	TCC [22]	□	79.72	81.12	81.35
	LAV [30]	□	83.56	83.95	84.25
	ViViT [2]+LAV [30]	□	70.66	72.92	74.76
	VAVA [49]	□	83.89	84.23	84.48
	CASA [41]	▲	<u>88.55</u>	<u>91.87</u>	<u>92.20</u>
	STGCN [75]+CASA [41]	▲	87.45	90.55	91.37
	LA2DS (Ours)	★	89.27	92.30	92.63
IKEA ASM	SAL [53]	□	21.68	21.72	22.14
	TCN [59]	□	25.17	25.70	26.80
	TCC [22]	□	24.74	25.22	26.46
	LAV [30]	□	<u>29.78</u>	29.85	30.43
	VAVA [49]	□	31.66	33.79	<u>32.91</u>
	CASA [41]	▲	21.32	31.52	31.06
		LA2DS (Ours)	★	26.43	<u>32.56</u>
H2O	TCC [22]	□	43.30	52.48	52.78
	LAV [30]	□	35.38	51.66	53.43
	CASA [41]	▲	<u>43.50</u>	<u>62.51</u>	<u>68.78</u>
		LA2DS (Ours)	★	52.86	64.58

Table 5. Phase classification results. Note that □ denotes direct RGB inputs, ▲ denotes 3D pose coordinate inputs, and ★ denotes 2D pose heatmap inputs. Best results are in **bold**, while second best ones are underlined.

	Method	Input	Progress.	τ
Penn Action	SAL [53]	□	0.6960	0.7612
	TCN [59]	□	0.7217	0.8120
	TCC [22]	□	0.6638	0.7012
	LAV [30]	□	0.6613	0.8047
	ViViT [2]+LAV [30]	□	0.7681	0.7059
	VAVA [49]	□	0.7091	0.8053
	CASA [41]	▲	0.9449	<u>0.9728</u>
	STGCN [75]+CASA [41]	▲	0.9061	0.9156
	LA2DS (Ours)	★	<u>0.9348</u>	0.9887
H2O	LAV [30]	□	0.5913	0.5323
	CASA [41]	▲	<u>0.9107</u>	<u>0.9438</u>
		LA2DS (Ours)	★	0.9280

Table 6. Phase progression and Kendall’s tau results. Note that □ denotes direct RGB inputs, ▲ denotes 3D pose coordinate inputs, and ★ denotes 2D pose heatmap inputs. Best results are in **bold**, while second best ones are underlined.

phase progression. This suggests that our method is capable of capturing dependencies between skeletons across sequences, which play a crucial role for temporal alignment.

	Method	Input	AP@5	AP@10	AP@15
Penn Action	SAL [53]	□	76.04	75.77	75.61
	TCN [59]	□	77.84	77.51	77.28
	TCC [22]	□	76.74	76.27	75.88
	LAV [30]	□	79.13	78.98	78.90
	ViViT [2]+LAV [30]	□	87.58	83.07	80.16
	VAVA [49]	□	81.52	80.47	80.67
	CASA [41]	▲	89.90	89.44	<u>89.07</u>
	STGCN [75]+CASA [41]	▲	<u>90.32</u>	<u>89.56</u>	88.41
	LA2DS (Ours)	★	93.07	91.84	91.35
IKEA ASM	SAL [53]	□	15.15	14.90	14.72
	TCN [59]	□	19.15	19.19	19.33
	TCC [22]	□	19.80	19.64	19.68
	LAV [30]	□	23.89	23.65	23.56
	VAVA [49]	□	<u>29.58</u>	28.74	28.48
	CASA [41]	▲	28.92	<u>28.88</u>	<u>28.61</u>
	LA2DS (Ours)	★	32.44	31.89	31.56
H2O	LAV [30]	□	47.55	45.56	44.61
	CASA [41]	▲	<u>60.13</u>	<u>59.44</u>	<u>59.01</u>
	LA2DS (Ours)	★	67.51	63.11	61.75

Table 7. Fine-grained frame retrieval results. Note that □ denotes direct RGB inputs, ▲ denotes 3D pose coordinate inputs, and ★ denotes 2D pose heatmap inputs. Best results are in **bold**, while second best ones are underlined.

4.2.3 Fine-Grained Frame Retrieval Results

Here, we examine the performance of our learned representations for fine-grained frame retrieval on Penn Action, IKEA ASM, and H2O, and compare it with previous methods as illustrated in Tab. 7. Following [30], our experimental setup involves using one video from the validation set as the query video, while the remaining videos in the validation set serve as the support set. To retrieve K most similar frames in the support set for each query frame in the query video, we find K nearest neighbors in the embedding space. We then calculate Average Precision at K , which represents the percentage of the K retrieved frames with the same action phase label as the query frame. It is obvious from Tab. 7 that our method achieves the best results, outperforming all competing methods across all datasets and all metrics. The results in Tab. 7 validate the effectiveness of our learned representations, which capture dependencies between joints in the same skeleton as well as dependencies between skeletons in the same sequence, for fine-grained frame retrieval.

4.3. Multi-Modality Fusion

Representing skeletons as heatmaps make it convenient to fuse with other modalities which have grid structures such as RGB videos, optical flows, and depth maps. In this section, we use both skeleton heatmaps and RGB videos as

	Method	Input	Class.	Progress.	τ	Retriev.
Penn Action	LAV [30]	□	84.25	0.6613	0.8047	78.90
	VAVA [49]	□	84.48	0.7091	0.8053	80.67
	CASA [41]	▲	92.20	<u>0.9449</u>	0.9728	89.07
	LA2DS (Ours)	★	<u>92.63</u>	0.9348	<u>0.9887</u>	<u>91.35</u>
	LA2DS (Ours)	□	88.58	0.8891	0.9625	81.08
	LA2DS (Ours)	★, □	93.57	0.9507	0.9903	92.15

Table 8. Multi-modality fusion results. Note that □ denotes direct RGB inputs, ▲ denotes 3D pose coordinate inputs, and ★ denotes 2D pose heatmap inputs. Best results are in **bold**, while second best ones are underlined.

inputs and perform late fusion. In particular, our RGB+Pose model begins with separate encoders which respectively map the original skeleton heatmaps H and the augmented skeleton heatmaps H' to features U_H and U'_H , and respectively map the original video frames F and the augmented video frames F' to features U_F and U'_F . We then fuse U_H and U_F together to obtain the combined features U for the original sequences, and fuse U'_H and U'_F together to obtain the combined features U' for the augmented sequences. The fused features U and U' are then passed to the projection heads before being used to perform matching and compute the loss as in Fig. 2. We first train the encoders for each modality separately using the single-modality alignment loss, and then train them jointly with late fusion. Tab. 8 presents the fusion results on Penn Action only. Due to space constraints, please refer to the supplementary material for the complete model architecture and results on all metrics and datasets. From the results, it is evident that our RGB+Pose model achieves the best performance across all metrics and datasets, establishing the state-of-the-art. This confirms the complementary benefit of multi-modality inputs for fine-grained human activity understanding tasks.

5. Conclusion

We present a novel 2D skeleton-based self-supervised temporal video alignment framework for fine-grained human activity understanding. In particular, we propose to take 2D skeleton heatmaps as input and employ a video transformer on 2D skeleton heatmaps which performs self-attention both in the spatial and temporal domains. This is in contrast with the state-of-the-art method of CASA, which directly processes 3D skeleton coordinates and does not conduct self-attention in the spatial domain. In addition, for self-supervised learning, we exploit simple heatmap augmentation techniques based on 2D skeletons. Our approach achieves not only better accuracy but also higher robustness against noisy and missing keypoints than CASA. Moreover, we show superior performance of our approach over previous methods on several fine-grained human activity un-

derstanding tasks on Penn Action, IKEA ASM, and H2O datasets. Lastly, our multi-modality version establishes the state-of-the-art on all metrics and datasets. To our best knowledge, our work is the first to exploit 2D skeleton heatmap inputs and the first to explore multi-modality fusion for temporal video alignment.

A. Supplementary Material

In this supplementary material, we first provide the details of our implementation in Sec. A.1. We then present the complete RGB+Pose network architecture and results on all metrics and datasets in Sec. A.2. Next, a number of quantitative results are included in Secs. A.3, A.4, A.5, A.6, and A.7, namely, comparison with a fusion baseline, using projected vs. estimated 2D poses, adding a recent augmentation technique, using predicted vs. ground truth heatmaps, and effects of different augmentations. Lastly, we show some qualitative results in Sec. A.8 and discuss the societal impacts of our work in Sec. A.9.

A.1. Implementation Details

Hyperparameter Settings. Tab. 9 includes a summary of our hyperparameter settings. We follow the same hyperparameter settings used in CASA [41], e.g., frames per second, batch size, temperature, learning rate, and weight decay. We keep the augmentation probability the same as CASA [41]. However, we adjust the noise standard deviation to 0.1 radian for orientation augmentation and 1 heatmap pixel for position augmentation, since our augmentation techniques are conducted on 2D skeletons/heatmaps. For CASA [41], the input vector length increases linearly with the number of keypoints and the number of objects (i.e., humans, hands) involved in each dataset. In contrast, our approach relies on the same heatmap spatial dimension of 30×30 for all datasets, demonstrating better scalability. In addition, for our self-attention module, we follow the same hyperparameter settings used in ViViT [2], except that we reduce the patch size to 10×10 and the transformer output dimension to 192 since our heatmap spatial dimension is small (i.e., 30×30).

Computing Resources. All of our experiments are performed with a single Nvidia A100 SXM4 GPU on Lambda Cloud.

A.2. Multi-Modality Fusion

We first provide the complete RGB+Pose network architecture in Fig. 5. Our RGB+Pose model first includes different encoders for mapping the original skeleton heatmaps H and the augmented skeleton heatmaps H' to features U_H and U'_H respectively, and mapping the original video frames F and the augmented video frames F' to features U_F and U'_F respectively. For video frame augmentation,

Hyperparameter	Value
Frames per second	20 (Penn Action), 30 (H2O, IKEA ASM)
Batch size	64 (Penn Action), 32 (H2O), 4 (IKEA ASM)
Temperature	0.1
Learning rate	$3e-3$ (Penn Action), $3e-4$ (H2O), $3e-2$ (IKEA ASM)
Weight decay	0.5
Augmentation probability	0.3 (flipping, orientation, position), 0.5 (temporal)
Noise standard deviation	0.1 radian (orientation), 1 heatmap pixel (position)
Heatmap spatial dimension	30×30
Patch size	10×10
Transformer output dimension	192
Optimizer	ADAM
Scheduler	MultiStepLR
Scheduler interval	Epoch

Table 9. Hyperparameter settings.

we perform temporal augmentation, brightness augmentation, contrast augmentation, and horizontal flipping. Next, U_H and U_F are fused together to yield the combined features U for the original sequences, and U'_H and U'_F are fused together to yield the combined features U' for the augmented sequences. Our fusion module includes concatenating the feature vectors and a linear layer to reduce the concatenated feature vector to the original size of 192. The fused features U and U' are then fed to the projection heads to obtain the final features Z and Z' which are used to perform matching and compute the loss. To train our RGB+Pose model, we perform two-stage training to avoid overfitting, i.e., we first train the encoders for each modality separately using the single-modality alignment loss, and then train them jointly with late fusion.

In addition, the complete multi-modality fusion results on all metrics and datasets are presented in Tab. 10. As it can be seen from the results, our multi-modality model achieves the best numbers across all metrics and datasets, outperforming all the single-modality competing methods and baselines. Moreover, our Pose-only model obtains the second best results in general on Penn Action and H2O, while often having worse results than our RGB-only model on IKEA ASM. Lastly, our RGB+Pose fusion results establish the state-of-the-art and confirm the complementary benefit of multi-modality inputs for fine-grained human activity understanding tasks.

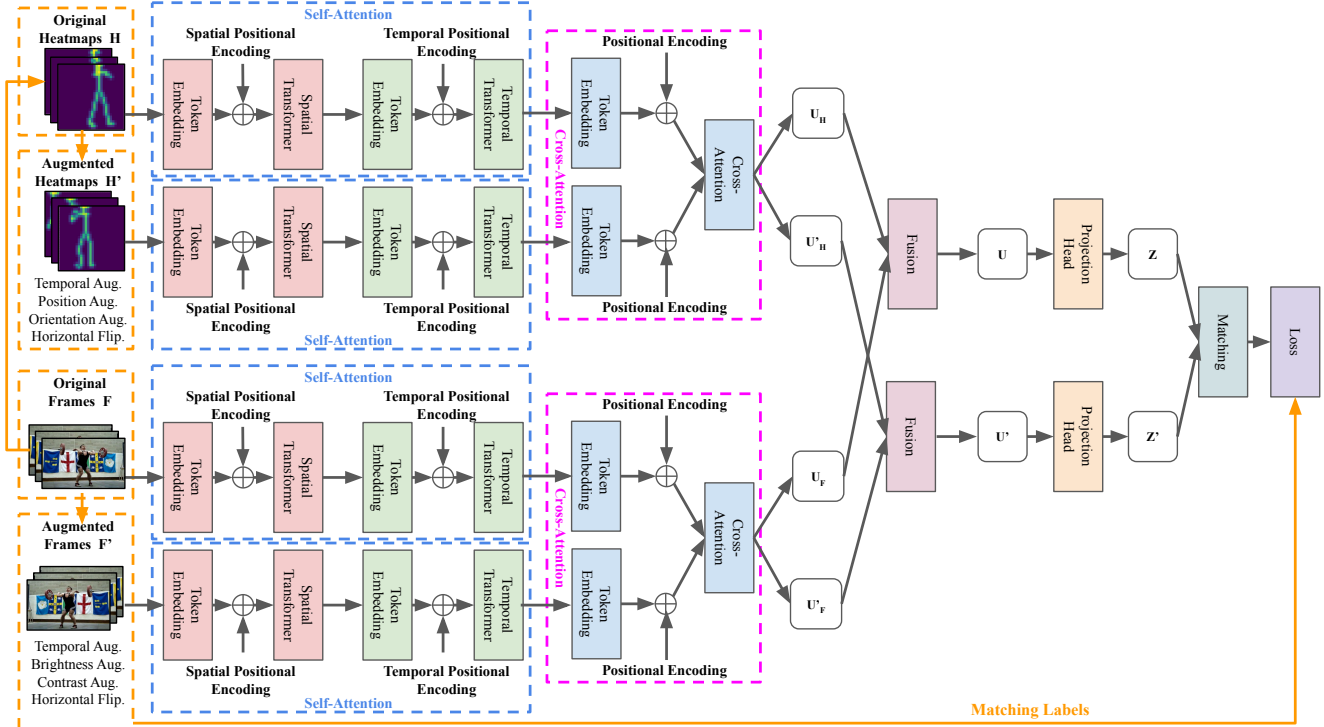


Figure 5. Our RGB+Pose network architecture.

	Method	Input	Acc@0.1	Acc@0.5	Acc@1.0	Progress	τ	AP@5	AP@10	AP@15
Penn Action	LAV [30]	□	83.56	83.95	84.25	0.6613	0.8047	79.13	78.98	78.90
	VAVA [49]	□	83.89	84.23	84.48	0.7091	0.8053	81.52	80.47	80.67
	CASA [41]	▲	88.55	91.87	92.20	<u>0.9449</u>	0.9728	89.90	89.44	89.07
	LA2DS (Ours)	★	<u>89.27</u>	<u>92.30</u>	<u>92.63</u>	0.9348	<u>0.9887</u>	<u>93.07</u>	<u>91.84</u>	<u>91.35</u>
	LA2DS (Ours)	□	84.75	86.91	88.58	0.8891	0.9625	84.81	82.16	81.08
	LA2DS (Ours)	★, □	90.22	93.02	93.57	0.9507	0.9903	93.63	92.25	92.15
IKEA ASM	LAV [30]	□	29.78	29.85	30.43	-	-	23.89	23.65	23.56
	VAVA [49]	□	<u>31.66</u>	<u>33.79</u>	32.91	-	-	29.58	28.74	28.48
	CASA [41]	▲	21.32	31.52	31.06	-	-	28.92	28.88	28.61
	LA2DS (Ours)	★	26.43	32.56	34.73	-	-	32.44	<u>31.89</u>	31.56
	LA2DS (Ours)	□	28.31	32.98	<u>35.55</u>	-	-	<u>32.65</u>	31.63	<u>31.60</u>
	LA2DS (Ours)	★, □	31.74	34.51	36.18	-	-	33.08	32.25	32.17
H2O	LAV [30]	□	35.38	51.66	53.43	0.5913	0.5323	47.55	45.56	44.61
	CASA [41]	▲	43.50	62.51	68.78	0.9107	0.9438	60.13	59.44	59.01
	LA2DS (Ours)	★	<u>52.86</u>	<u>64.58</u>	<u>70.12</u>	<u>0.9280</u>	<u>0.9670</u>	<u>67.51</u>	<u>63.11</u>	<u>61.75</u>
	LA2DS (Ours)	□	48.08	63.26	68.85	0.9113	0.9478	63.33	61.87	60.12
	LA2DS (Ours)	★, □	54.55	65.96	70.65	0.9367	0.9737	70.33	67.76	63.23

Table 10. Multi-modality fusion results. Note that □ denotes direct RGB inputs, ▲ denotes 3D pose coordinate inputs, and ★ denotes 2D pose heatmap inputs. Best results are in **bold**, while second best ones are underlined.

A.3. Comparison with a Fusion Baseline

Our work is the first to explore multi-modality fusion for video alignment. For comparison purposes, we ex-

	Method	Input	Acc@0.1	Acc@0.5	Acc@1.0	Progress.	τ	AP@5	AP@10	AP@15
A	CASA	▲, □	88.97	92.55	92.90	0.9494	0.9808	91.74	90.97	90.25
	LA2DS	*, □	90.22	93.02	93.57	0.9507	0.9903	93.63	92.25	92.15
B	Projected	*	89.27	92.30	92.63	0.9348	0.9887	93.07	91.84	91.35
	OpenPose	*	96.41	96.81	96.95	0.9563	0.9905	95.65	95.43	95.34
C	w/o MaskOut	*, □	90.22	93.02	93.57	0.9507	0.9903	93.63	92.25	92.15
	MaskOut	*, □	89.95	92.22	92.91	0.9445	0.9899	92.77	92.65	92.43
D	Predicted	*	26.43	32.56	34.73	-	-	32.44	31.89	31.56
	Ground Truth	*	27.32	34.39	35.86	-	-	34.61	33.69	33.49

Table 11. (A) Comparison with a fusion baseline. (B) Using projected vs. estimated 2D poses. (C) Adding a recent augmentation. (D) Using predicted vs. ground truth heatmaps. Note that □ denotes direct RGB inputs, ▲ denotes 3D pose coordinate inputs, and * denotes 2D pose heatmap inputs. (A-C) are conducted on Penn Action, while (D) is performed on IKEA ASM since ground truth 2D poses are not available on Penn Action. Best results are in **bold**.

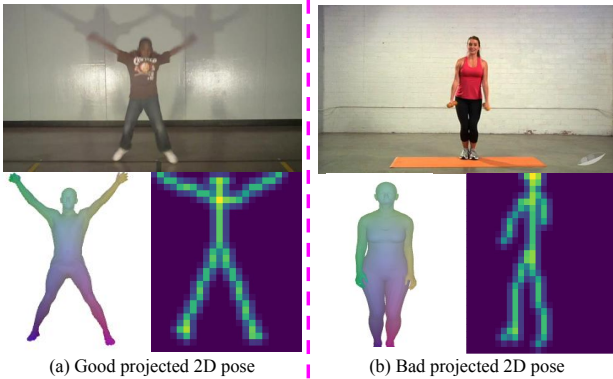


Figure 6. Examples of our projected 2D poses. In (a) or (b), RGB frame is plotted at the top, while 3D pose provided by CASA and our projected 2D pose are visualized at the bottom.

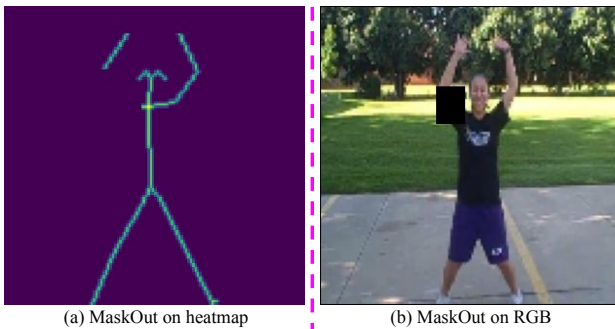


Figure 7. Examples of MaskOut augmentation.

tend CASA by first adding branches with RGB inputs (i.e., RGB features extracted by pre-trained ResNet) and MLP encoders and then performing RGB+3D skeleton fusion via late fusion (similar to our RGB+2D skeleton fusion model in Fig. 5). Tab. 11(A) shows results of the fusion baseline

on Penn Action. It is evident from the results that our fusion model outperforms the fusion baseline.

A.4. Using Projected vs. Estimated 2D Poses

We presents results of using OpenPose 2D poses on Penn Action in Tab. 11(B). We use OpenPose 2D poses since CASA uses FrankMocap 3D poses, which are computed from OpenPose 2D poses. It is clear from the results that using OpenPose 2D poses outperforms using our projected 2D poses. This is likely because our projected 2D poses have deviations/deformations due to orthographic projection (camera intrinsics/extrinsics are not provided on Penn Action). Fig. 6 illustrates examples of our projected 2D poses obtained via orthographic projection.

A.5. Adding a Recent Augmentation Technique

So far, our 2D skeleton heatmap augmentations include temporal augmentation, position augmentation, orientation augmentation, and horizontal flipping, while our video frame augmentations include temporal augmentation, brightness augmentation, contrast augmentation, and horizontal flipping. In this section, we experiment with adding a recent augmentation method on both RGB and heatmap inputs, i.e., masking out a random limb along with the rectangular region containing it. Fig. 7 plots examples of MaskOut augmentation, while results of adding MaskOut augmentation on Penn Action are shown in Tab. 11(C). From the results, adding MaskOut augmentation slightly improves the performance on the retrieval task, while lowering the performance on the remaining tasks.

A.6. Using Predicted vs. Ground Truth Heatmaps

We now examine the performance of using predicted heatmaps and using ground truth heatmaps. Our predicted heatmaps are derived from 2D skeletons which are projected from 3D skeletons provided by CASA (i.e., pre-

	Method	Class.	Progress.	τ
H2O	No Aug.	63.12	0.9080	0.9350
	w/o Temp. Aug.	64.82	0.9194	0.9551
	w/o Ori. Aug.	67.40	0.9203	0.9603
	w/o Pos. Aug.	<u>69.18</u>	<u>0.9228</u>	0.9626
	w/o Hor. Flip.	67.93	0.9193	<u>0.9642</u>
	All	70.12	0.9280	0.9670

Table 12. Effects of different augmentations. Best results are in **bold**, while second best ones are underlined.

dicted by FrankMocap), while our ground truth heatmaps are derived from ground truth 2D skeletons provided by IKEA ASM. Tab. 11(D) presents results of using predicted heatmaps and using ground truth heatmaps on IKEA ASM. It can be seen from the results that using ground truth heatmaps leads to better results than using predicted heatmaps.

A.7. Effects of Different Augmentations

Tab. 12 provides the ablation results on various data augmentation techniques. It can be seen from Tab. 12 that utilizing all augmentations simultaneously yields the best performance across all metrics, whereas eliminating all augmentations leads to a significant performance drop. While removing orientation augmentation and horizontal flipping causes a drop of roughly 3% in classification accuracy, removing position augmentation reduces the accuracy by 1%. In addition, the absence of temporal augmentation has the greatest impact on classification accuracy among all augmentations, underscoring the importance of temporal information.

A.8. Qualitative Results

Firstly, Figs. 8 and 9 illustrate the alignment results of our approach and CASA [41] between two *pullups* sequences and two *bowling* sequences. It is evident from the figures that LA2DS achieves more seamless alignment results than CASA [41]. Our method learns interactions between skeletons across the sequences to align them in time effectively.

Moreover, Fig. 10 shows the fine-grained frame retrieval results of our approach, CASA [41], and LAV [30] on *clean_and_jerk* and *jumping_jacks* sequences. LA2DS extracts useful spatiotemporal and contextual features within each sequence, resulting in more accurate fine-grained frame retrieval results than CASA [41] and LAV [30], as can be seen in Fig. 10.

Finally, we show the alignment results, i.e., framewise correspondences, between two *tennis_serve* sequences in Fig. 11. Our method achieves a more seamless alignment as compared to CASA [41]. In Fig. 12, the learned

embeddings of two *baseball_pitch* sequences are plotted using t-SNE [68]. LA2DS successfully aligns the sequences temporally, as evident by the proximity of temporally close frames in the embedding space. LA2DS outperforms CASA [41] in terms of capturing the temporal context and aligning the sequences in time.

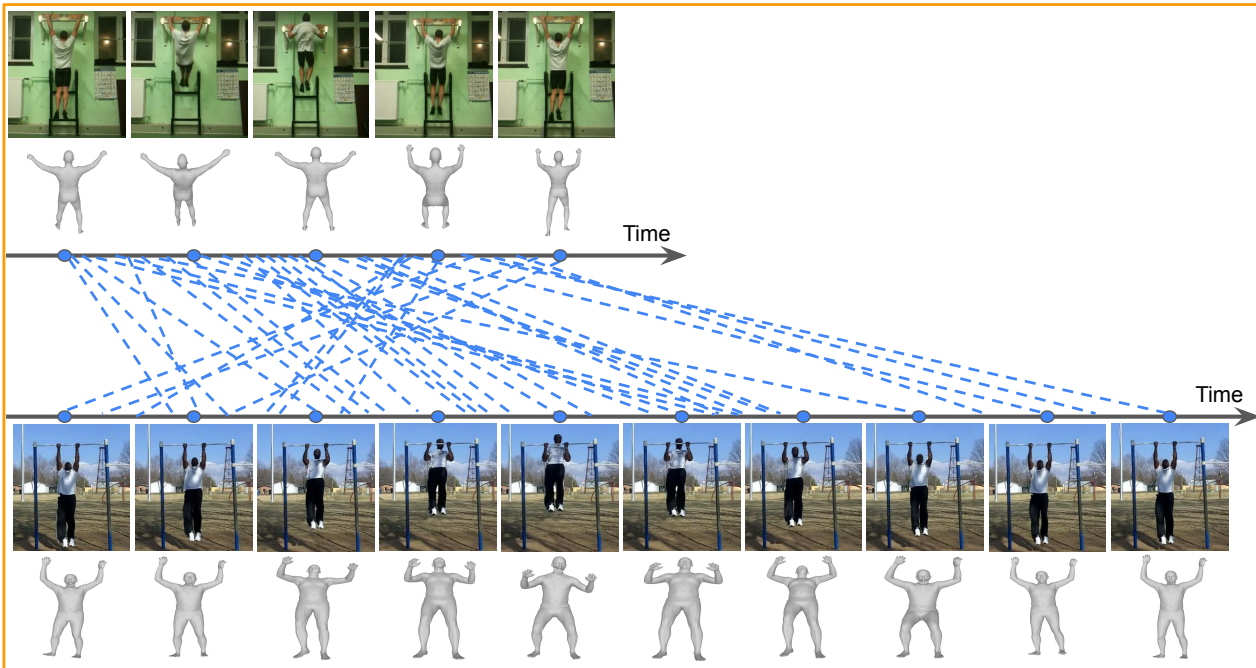
A.9. Societal Impacts

Our sequence alignment method offers valuable applications including frontline worker training and assistance. In particular, frontline workers could benefit from guidance provided by models generated from expert demonstration videos in various domains from factory assembly to medical surgery. However, we also acknowledge the potential for misuse in surveillance and monitoring of individuals. This may raise privacy concerns, emphasizing the importance of responsible AI principles to guide the use of this technology.

References

- [1] Unaiza Ahsan, Chen Sun, and Irfan Essa. Discrimnet: Semi-supervised action recognition from videos using generative adversarial networks. *arXiv preprint*, 2018. 2
- [2] Anurag Arnab, Mostafa Dehghani, Georg Heigold, Chen Sun, Mario Lučić, and Cordelia Schmid. Vivit: A video vision transformer. In *Proceedings of the IEEE/CVF International Conference on Computer Vision*, pages 6836–6846, 2021. 2, 4, 5, 7, 8, 9
- [3] Sadjad Asghari-Esfeden, Mario Szanier, and Octavia Camps. Dynamic motion representation for human action recognition. In *Proceedings of the IEEE/CVF winter conference on applications of computer vision*, pages 557–566, 2020. 3
- [4] Yizhak Ben-Shabat, Xin Yu, Fatemehsadat Saleh, Dylan Campbell, Cristian Rodriguez-Opazo, Hongdong Li, and Stephen Gould. The ikea asm dataset: Understanding people assembling furniture through actions, objects, and pose. In *arXiv preprint*, 2020. 5
- [5] Sagie Benaim, Ariel Ephrat, Oran Lang, Inbar Mosseri, William T Freeman, Michael Rubinstein, Michal Irani, and Tali Dekel. Speednet: Learning the speediness in videos. In *Proceedings of the IEEE/CVF Conference on Computer Vision and Pattern Recognition*, pages 9922–9931, 2020. 2
- [6] Carlos Caetano, Jessica Sena, François Brémond, Jeferson A Dos Santos, and William Robson Schwartz. Skelemotion: A new representation of skeleton joint sequences based on motion information for 3d action recognition. In *2019 16th IEEE international conference on advanced video and signal based surveillance (AVSS)*, pages 1–8. IEEE, 2019. 3
- [7] Jinmiao Cai, Nianjuan Jiang, Xiaoguang Han, Kui Jia, and Jiangbo Lu. Jolo-gcn: mining joint-centered light-weight information for skeleton-based action recognition. In *Proceedings of the IEEE/CVF winter conference on applications of computer vision*, pages 2735–2744, 2021. 3
- [8] Fabio M Carlucci, Antonio D’Innocente, Silvia Bucci, Barbara Caputo, and Tatiana Tommasi. Domain generalization

CASA



LA2DS

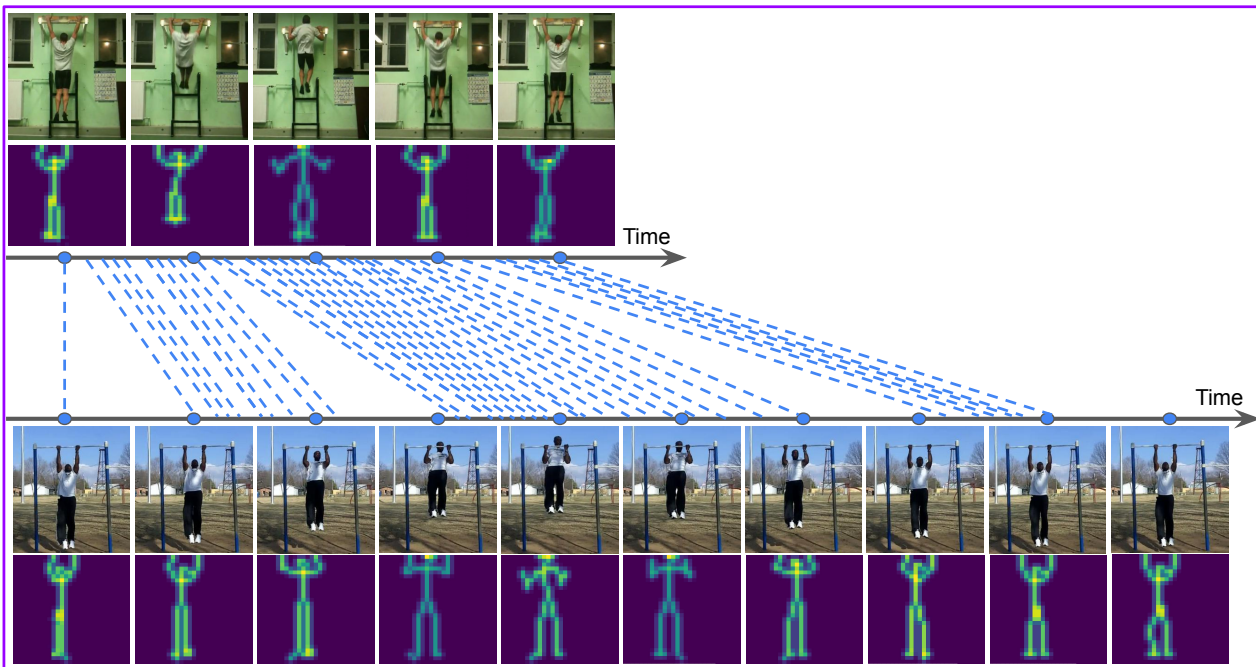
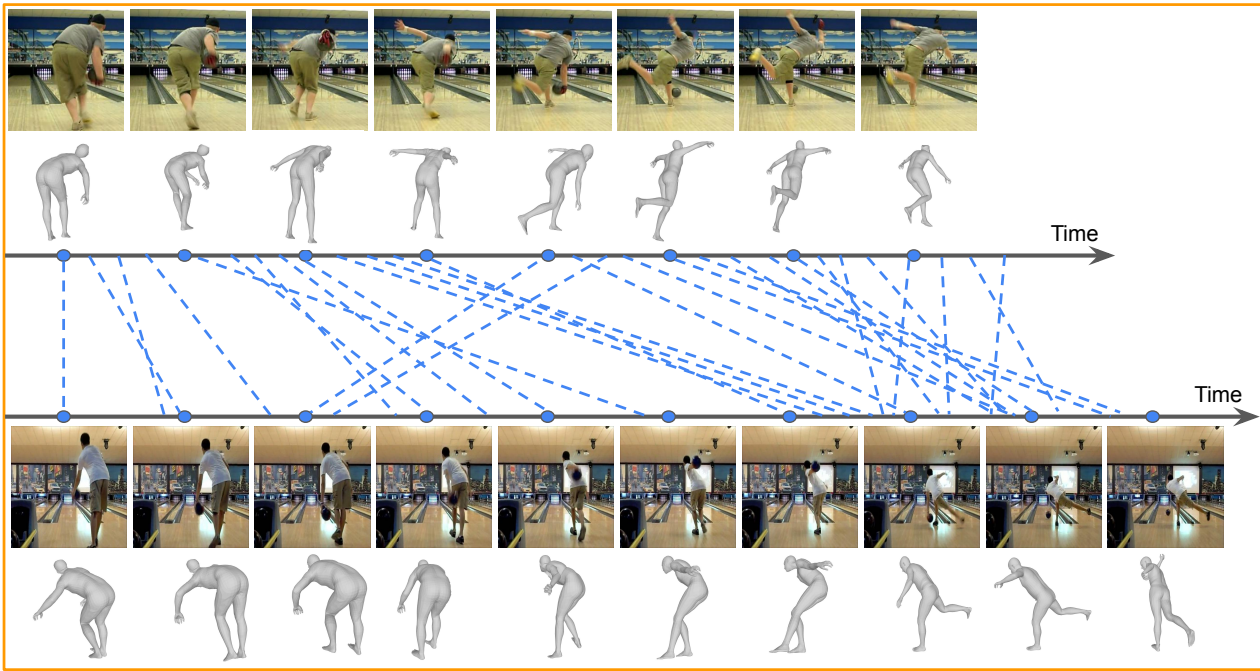


Figure 8. Alignment results of two *pullups* sequences. Blue lines indicate where frames in both sequences match.

by solving jigsaw puzzles. In *Proceedings of the IEEE Conference on Computer Vision and Pattern Recognition*, pages 2229–2238, 2019. 2

[9] Mathilde Caron, Piotr Bojanowski, Armand Joulin, and Matthijs Douze. Deep clustering for unsupervised learning of visual features. In *Proceedings of the European Confer-*

CASA



LA2DS

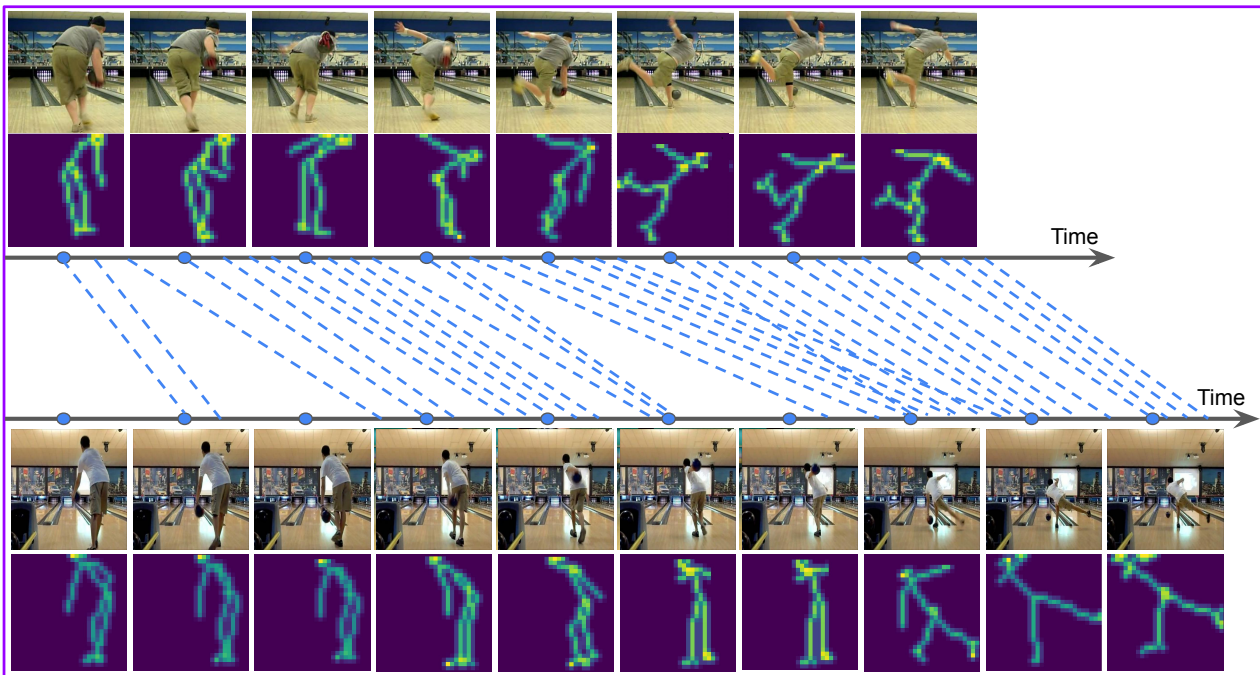


Figure 9. Alignment results of two *bowling* sequences. Blue lines indicate where frames in both sequences match.

ence on Computer Vision (ECCV), pages 132–149, 2018. 2

[10] Mathilde Caron, Piotr Bojanowski, Julien Mairal, and Armand Joulin. Unsupervised pre-training of image features

on non-curved data. In *Proceedings of the IEEE/CVF International Conference on Computer Vision*, pages 2959–2968, 2019. 2

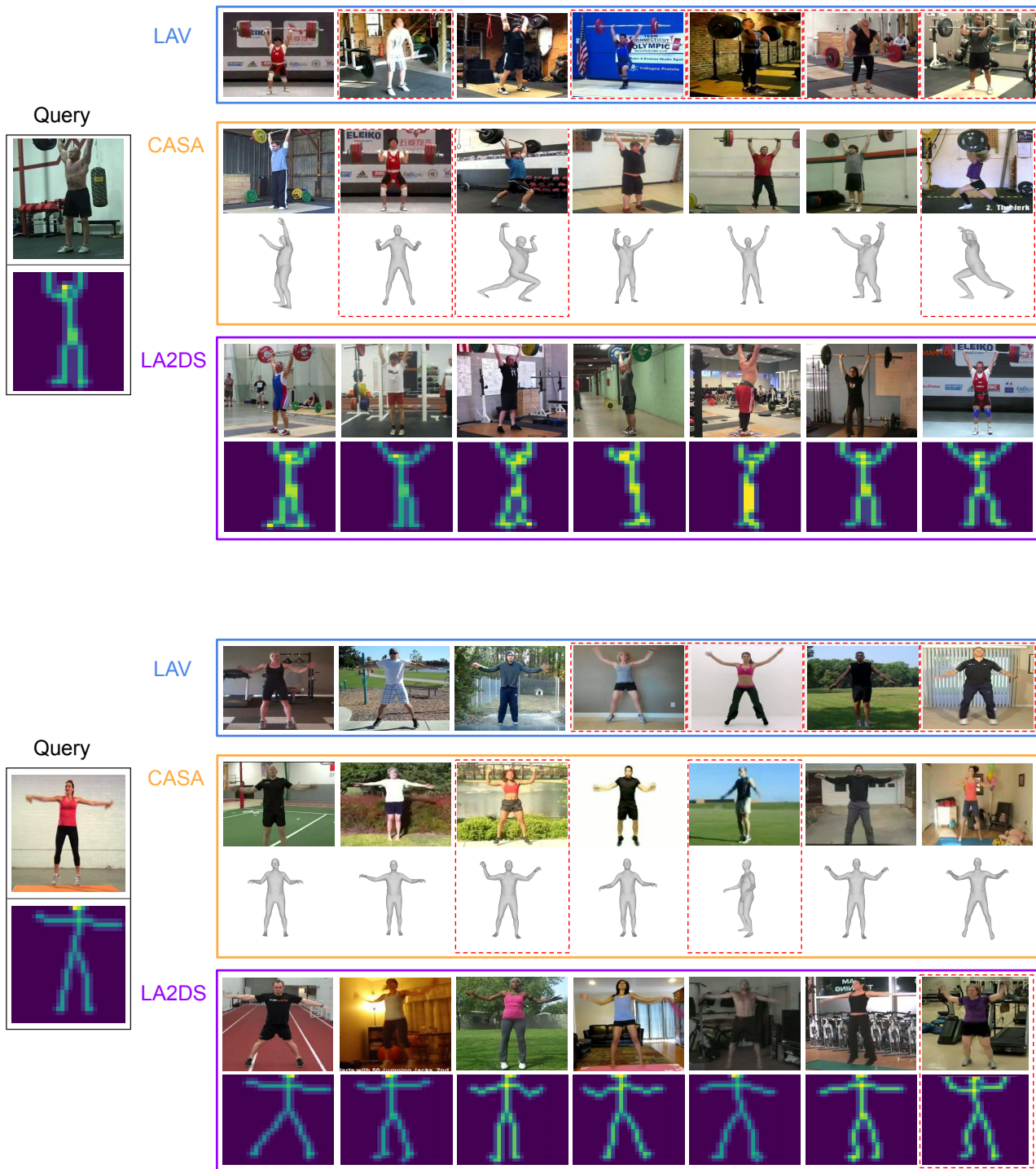


Figure 10. Fine-grained frame retrieval results on *clean_and_jerk* and *jumping_jacks* sequences with $k = 7$. Mismatches between the action phase of the query frame and those of the retrieved frames are indicated by red boxes.

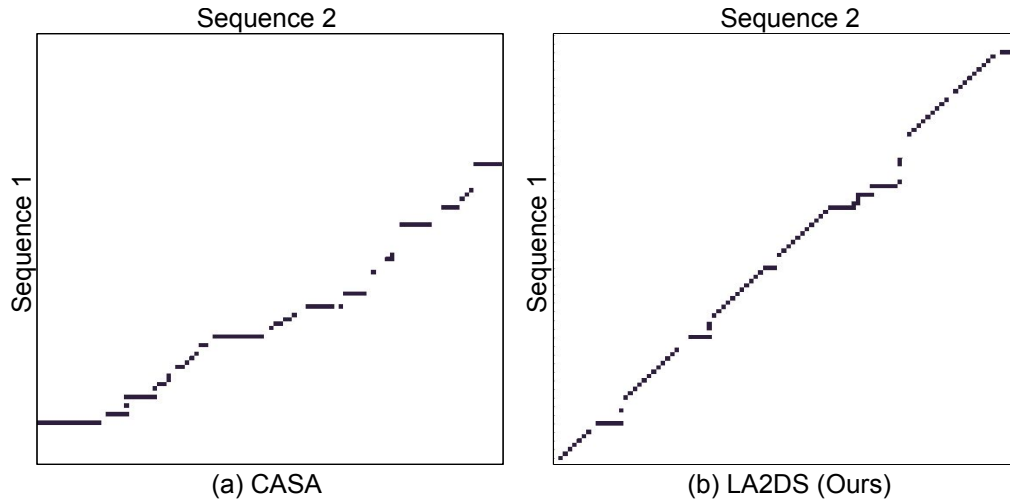


Figure 11. Alignment results of two *tennis_serve* videos. Black dots indicate alignment results.

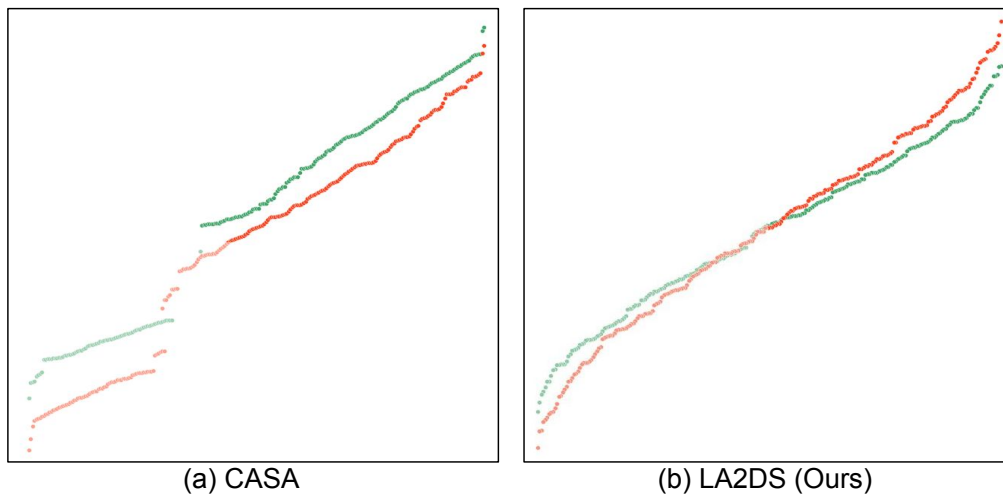


Figure 12. t-SNE visualizations of learned embeddings of two *baseball_pitch* videos. The opacity of the color denotes the temporal frame index from the first to the last.

- [11] Mathilde Caron, Ishan Misra, Julien Mairal, Priya Goyal, Piotr Bojanowski, and Armand Joulin. Unsupervised learning of visual features by contrasting cluster assignments. *Advances in neural information processing systems*, 33:9912–9924, 2020. 2
- [12] Ting Chen, Simon Kornblith, Mohammad Norouzi, and Geoffrey Hinton. A simple framework for contrastive learning of visual representations. In *International conference on machine learning*, pages 1597–1607. PMLR, 2020. 2, 5
- [13] Xinlei Chen and Kaiming He. Exploring simple siamese representation learning. In *Proceedings of the IEEE/CVF conference on computer vision and pattern recognition*, pages 15750–15758, 2021. 2
- [14] Yuxin Chen, Ziqi Zhang, Chunfeng Yuan, Bing Li, Ying Deng, and Weiming Hu. Channel-wise topology refinement graph convolution for skeleton-based action recognition. In *Proceedings of the IEEE/CVF International Conference on Computer Vision*, pages 13359–13368, 2021. 3
- [15] Vasileios Choutas, Philippe Weinzaepfel, Jérôme Revaud, and Cordelia Schmid. Potion: Pose motion representation for action recognition. In *Proceedings of the IEEE conference on computer vision and pattern recognition*, pages 7024–7033, 2018. 3
- [16] Marco Cuturi. Sinkhorn distances: Lightspeed computation of optimal transport. *Advances in neural information processing systems*, 26, 2013. 2, 3
- [17] Marco Cuturi and Mathieu Blondel. Soft-dtw: a differentiable loss function for time-series. In *International conference on machine learning*, pages 894–903. PMLR, 2017. 2, 3
- [18] Srijan Das, Saurav Sharma, Rui Dai, Francois Bremond, and Monique Thonnat. Vpn: Learning video-pose embedding for activities of daily living. In *Computer Vision—ECCV*

- 2020: *16th European Conference, Glasgow, UK, August 23–28, 2020, Proceedings, Part IX 16*, pages 72–90. Springer, 2020. 3
- [19] Ishan Dave, Rohit Gupta, Mamshad Nayeem Rizve, and Mubarak Shah. Tclr: Temporal contrastive learning for video representation. *Computer Vision and Image Understanding*, 219:103406, 2022. 2
- [20] Ali Diba, Vivek Sharma, Luc Van Gool, and Rainer Stiefelhagen. Dynamonet: Dynamic action and motion network. In *Proceedings of the IEEE International Conference on Computer Vision*, pages 6192–6201, 2019. 2
- [21] Haodong Duan, Yue Zhao, Kai Chen, Dahua Lin, and Bo Dai. Revisiting skeleton-based action recognition. In *Proceedings of the IEEE/CVF Conference on Computer Vision and Pattern Recognition*, pages 2969–2978, 2022. 2, 3
- [22] Debidatta Dwibedi, Yusuf Aytar, Jonathan Tompson, Pierre Sermanet, and Andrew Zisserman. Temporal cycle-consistency learning. In *Proceedings of the IEEE/CVF Conference on Computer Vision and Pattern Recognition (CVPR)*, June 2019. 1, 2, 3, 5, 7, 8
- [23] Christoph Feichtenhofer, Haoqi Fan, Bo Xiong, Ross Girshick, and Kaiming He. A large-scale study on unsupervised spatiotemporal representation learning. In *Proceedings of the IEEE/CVF Conference on Computer Vision and Pattern Recognition*, pages 3299–3309, 2021. 2
- [24] Basura Fernando, Hakan Bilen, Efstratios Gavves, and Stephen Gould. Self-supervised video representation learning with odd-one-out networks. In *Proceedings of the IEEE conference on computer vision and pattern recognition*, pages 3636–3645, 2017. 2
- [25] Spyros Gidaris, Praveer Singh, and Nikos Komodakis. Unsupervised representation learning by predicting image rotations. In *International Conference on Learning Representations*, 2018. 2
- [26] Ross Girshick. Fast r-cnn. In *Proceedings of the IEEE international conference on computer vision*, pages 1440–1448, 2015. 3
- [27] Ross Goroshin, Joan Bruna, Jonathan Tompson, David Eigen, and Yann LeCun. Unsupervised learning of spatiotemporally coherent metrics. In *Proceedings of the IEEE international conference on computer vision*, pages 4086–4093, 2015. 2
- [28] Jean-Bastien Grill, Florian Strub, Florent Althé, Corentin Tallec, Pierre Richemond, Elena Buchatskaya, Carl Doersch, Bernardo Avila Pires, Zhaohan Guo, Mohammad Gheshlaghi Azar, et al. Bootstrap your own latent—a new approach to self-supervised learning. *Advances in neural information processing systems*, 33:21271–21284, 2020. 2
- [29] Pranay Gupta, Anirudh Thatipelli, Aditya Aggarwal, Shubh Maheshwari, Neel Trivedi, Sourav Das, and Ravi Kiran Sarvadevabhatla. Quo vadis, skeleton action recognition? *International Journal of Computer Vision*, 129(7):2097–2112, 2021. 3
- [30] Sanjay Haresh, Sateesh Kumar, Huseyin Coskun, Shahram N Syed, Andrey Konin, Zeeshan Zia, and Quoc-Huy Tran. Learning by aligning videos in time. In *Proceedings of the IEEE/CVF Conference on Computer Vision and Pattern Recognition*, pages 5548–5558, 2021. 1, 2, 3, 5, 7, 8, 10, 12
- [31] Kaiming He, Xiangyu Zhang, Shaoqing Ren, and Jian Sun. Deep residual learning for image recognition. In *Proceedings of the IEEE conference on computer vision and pattern recognition*, pages 770–778, 2016. 7
- [32] Alejandro Hernandez Ruiz, Lorenzo Porzi, Samuel Rota Bulò, and Francesc Moreno-Noguer. 3d cnns on distance matrices for human action recognition. In *Proceedings of the 25th ACM international conference on Multimedia*, pages 1087–1095, 2017. 3
- [33] Kai Hu, Jie Shao, Yuan Liu, Bhiksha Raj, Marios Savvides, and Zhiqiang Shen. Contrast and order representations for video self-supervised learning. In *Proceedings of the IEEE/CVF International Conference on Computer Vision*, pages 7939–7949, 2021. 2
- [34] Simon Jenni, Hailin Jin, and Paolo Favaro. Steering self-supervised feature learning beyond local pixel statistics. In *Proceedings of the IEEE/CVF Conference on Computer Vision and Pattern Recognition*, pages 6408–6417, 2020. 2
- [35] Will Kay, Joao Carreira, Karen Simonyan, Brian Zhang, Chloe Hillier, Sudheendra Vijayanarasimhan, Fabio Viola, Tim Green, Trevor Back, Paul Natsev, Mustafa Suleyman, and Andrew Zisserman. The kinetics human action video dataset. arXiv, 2017. 5
- [36] Qihong Ke, Mohammed Bennamoun, Senjian An, Ferdous Sohel, and Farid Boussaid. A new representation of skeleton sequences for 3d action recognition. In *Proceedings of the IEEE conference on computer vision and pattern recognition*, pages 3288–3297, 2017. 3
- [37] Dahun Kim, Donghyeon Cho, and In So Kweon. Self-supervised video representation learning with space-time cubic puzzles. In *Proceedings of the AAAI Conference on Artificial Intelligence*, volume 33, pages 8545–8552, 2019. 2
- [38] Diederik P Kingma and Jimmy Ba. Adam: A method for stochastic optimization. *arXiv preprint*, 2014. 5
- [39] Sateesh Kumar, Sanjay Haresh, Awais Ahmed, Andrey Konin, M Zeeshan Zia, and Quoc-Huy Tran. Unsupervised action segmentation by joint representation learning and online clustering. In *Proceedings of the IEEE/CVF Conference on Computer Vision and Pattern Recognition*, pages 20174–20185, 2022. 2
- [40] Taein Kwon, Bugra Tekin, Jan Stühmer, Federica Bogo, and Marc Pollefeys. H2o: Two hands manipulating objects for first person interaction recognition. In *Proceedings of the IEEE/CVF International Conference on Computer Vision (ICCV)*, pages 10138–10148, October 2021. 5
- [41] Taein Kwon, Bugra Tekin, Siyu Tang, and Marc Pollefeys. Context-aware sequence alignment using 4d skeletal augmentation. In *Proceedings of the IEEE/CVF Conference on Computer Vision and Pattern Recognition*, pages 8172–8182, 2022. 1, 2, 3, 4, 5, 6, 7, 8, 9, 10, 12
- [42] Gustav Larsson, Michael Maire, and Gregory Shakhnarovich. Learning representations for automatic colorization. In *European conference on computer vision*, pages 577–593. Springer, 2016. 2
- [43] Gustav Larsson, Michael Maire, and Gregory Shakhnarovich. Colorization as a proxy task for visual understanding. In *Proceedings of the IEEE Conference*

- on *Computer Vision and Pattern Recognition*, pages 6874–6883, 2017. 2
- [44] Hsin-Ying Lee, Jia-Bin Huang, Maneesh Singh, and Ming-Hsuan Yang. Unsupervised representation learning by sorting sequences. In *Proceedings of the IEEE International Conference on Computer Vision*, pages 667–676, 2017. 2
- [45] Chao Li, Qiaoyong Zhong, Di Xie, and Shiliang Pu. Co-occurrence feature learning from skeleton data for action recognition and detection with hierarchical aggregation. *arXiv preprint*, 2018. 3
- [46] Lilang Lin, Sijie Song, Wenhan Yang, and Jiaying Liu. Ms2l: Multi-task self-supervised learning for skeleton based action recognition. In *Proceedings of the 28th ACM International Conference on Multimedia*, pages 2490–2498, 2020. 2
- [47] Zeyi Lin, Wei Zhang, Xiaoming Deng, Cuixia Ma, and Hongan Wang. Image-based pose representation for action recognition and hand gesture recognition. In *2020 15th IEEE International Conference on Automatic Face and Gesture Recognition (FG 2020)*, pages 532–539. IEEE, 2020. 3
- [48] Hong Liu, Juanhui Tu, and Mengyuan Liu. Two-stream 3d convolutional neural network for skeleton-based action recognition. *arXiv preprint*, 2017. 3
- [49] Weizhe Liu, Bugra Tekin, Huseyin Coskun, Vibhav Vineet, Pascal Fua, and Marc Pollefeys. Learning to align sequential actions in the wild. In *Proceedings of the IEEE/CVF Conference on Computer Vision and Pattern Recognition*, pages 2181–2191, 2022. 1, 2, 3, 5, 7, 8, 10
- [50] Xialei Liu, Joost Van De Weijer, and Andrew D Bagdanov. Leveraging unlabeled data for crowd counting by learning to rank. In *Proceedings of the IEEE Conference on Computer Vision and Pattern Recognition*, pages 7661–7669, 2018. 2
- [51] Diogo C Luvizon, David Picard, and Hedi Tabia. 2d/3d pose estimation and action recognition using multitask deep learning. In *Proceedings of the IEEE conference on computer vision and pattern recognition*, pages 5137–5146, 2018. 3
- [52] Ishan Misra, C Lawrence Zitnick, and Martial Hebert. Shuffle and learn: unsupervised learning using temporal order verification. In *European Conference on Computer Vision*, pages 527–544. Springer, 2016. 2
- [53] Ishan Misra, C. Lawrence Zitnick, and Martial Hebert. Shuffle and learn: Unsupervised learning using temporal order verification. In Bastian Leibe, Jiri Matas, Nicu Sebe, and Max Welling, editors, *Computer Vision – ECCV 2016*, pages 527–544. Cham, 2016. Springer International Publishing. 5, 7, 8
- [54] Hossein Mobahi, Ronan Collobert, and Jason Weston. Deep learning from temporal coherence in video. In *Proceedings of the 26th Annual International Conference on Machine Learning*, pages 737–744, 2009. 2
- [55] Mehdi Noroozi, Hamed Pirsiavash, and Paolo Favaro. Representation learning by learning to count. In *Proceedings of the IEEE International Conference on Computer Vision*, pages 5898–5906, 2017. 2
- [56] Adam Paszke, Sam Gross, Soumith Chintala, Gregory Chanan, Edward Yang, Zachary DeVito, Zeming Lin, Alban Desmaison, Luca Antiga, and Adam Lerer. Automatic differentiation in pytorch. 2017. 5
- [57] Lyndsey C Pickup, Zheng Pan, Donglai Wei, YiChang Shih, Changshui Zhang, Andrew Zisserman, Bernhard Scholkopf, and William T Freeman. Seeing the arrow of time. In *Proceedings of the IEEE Conference on Computer Vision and Pattern Recognition*, pages 2035–2042, 2014. 2
- [58] Rui Qian, Tianjian Meng, Boqing Gong, Ming-Hsuan Yang, Huisheng Wang, Serge Belongie, and Yin Cui. Spatiotemporal contrastive video representation learning. In *Proceedings of the IEEE/CVF Conference on Computer Vision and Pattern Recognition*, pages 6964–6974, 2021. 2
- [59] Pierre Sermanet, Corey Lynch, Yevgen Chebotar, Jasmine Hsu, Eric Jang, Stefan Schaal, Sergey Levine, and Google Brain. Time-contrastive networks: Self-supervised learning from video. In *2018 IEEE International Conference on Robotics and Automation (ICRA)*, pages 1134–1141, 2018. 1, 2, 5, 7, 8
- [60] Chenyang Si, Xuecheng Nie, Wei Wang, Liang Wang, Tieniu Tan, and Jiashi Feng. Adversarial self-supervised learning for semi-supervised 3d action recognition. In *Computer Vision—ECCV 2020: 16th European Conference, Glasgow, UK, August 23–28, 2020, Proceedings, Part VII 16*, pages 35–51. Springer, 2020. 2
- [61] Yi-Fan Song, Zhang Zhang, Caifeng Shan, and Liang Wang. Stronger, faster and more explainable: A graph convolutional baseline for skeleton-based action recognition. In *proceedings of the 28th ACM international conference on multimedia*, pages 1625–1633, 2020. 3
- [62] Yi-Fan Song, Zhang Zhang, Caifeng Shan, and Liang Wang. Constructing stronger and faster baselines for skeleton-based action recognition. *IEEE transactions on pattern analysis and machine intelligence*, 45(2):1474–1488, 2022. 3
- [63] Nitish Srivastava, Elman Mansimov, and Ruslan Salakhudinov. Unsupervised learning of video representations using lstms. In *International conference on machine learning*, pages 843–852, 2015. 2
- [64] Kun Su, Xiulong Liu, and Eli Shlizerman. Predict & cluster: Unsupervised skeleton based action recognition. In *Proceedings of the IEEE/CVF Conference on Computer Vision and Pattern Recognition*, pages 9631–9640, 2020. 2
- [65] Yukun Su, Guosheng Lin, and Qingyao Wu. Self-supervised 3d skeleton action representation learning with motion consistency and continuity. In *Proceedings of the IEEE/CVF international conference on computer vision*, pages 13328–13338, 2021. 2
- [66] Jiaming Sun, Zehong Shen, Yuang Wang, Hujun Bao, and Xiaowei Zhou. Loftr: Detector-free local feature matching with transformers. In *Proceedings of the IEEE/CVF conference on computer vision and pattern recognition*, pages 8922–8931, 2021. 5
- [67] Ke Sun, Bin Xiao, Dong Liu, and Jingdong Wang. Deep high-resolution representation learning for human pose estimation. In *Proceedings of the IEEE/CVF conference on computer vision and pattern recognition*, pages 5693–5703, 2019. 3
- [68] Laurens van der Maaten and Geoffrey Hinton. Visualizing data using t-sne. In *Journal of Machine Learning Research*, volume 9, pages 2579–2605, 2008. 12

- [69] Ashish Vaswani, Noam Shazeer, Niki Parmar, Jakob Uszkoreit, Llion Jones, Aidan N Gomez, Łukasz Kaiser, and Illia Polosukhin. Attention is all you need. *Advances in neural information processing systems*, 30, 2017. 2
- [70] Carl Vondrick, Hamed Pirsiavash, and Antonio Torralba. Generating videos with scene dynamics. In *Advances in neural information processing systems*, pages 613–621, 2016. 2
- [71] Jiangliu Wang, Jianbo Jiao, and Yun-Hui Liu. Self-supervised video representation learning by pace prediction. In *Computer Vision–ECCV 2020: 16th European Conference, Glasgow, UK, August 23–28, 2020, Proceedings, Part XVII 16*, pages 504–521. Springer, 2020. 2
- [72] Donglai Wei, Joseph J Lim, Andrew Zisserman, and William T Freeman. Learning and using the arrow of time. In *Proceedings of the IEEE conference on computer vision and pattern recognition*, pages 8052–8060, 2018. 2
- [73] Dejing Xu, Jun Xiao, Zhou Zhao, Jian Shao, Di Xie, and Yueting Zhuang. Self-supervised spatiotemporal learning via video clip order prediction. In *Proceedings of the IEEE Conference on Computer Vision and Pattern Recognition*, pages 10334–10343, 2019. 2
- [74] An Yan, Yali Wang, Zhifeng Li, and Yu Qiao. Pa3d: Pose-action 3d machine for video recognition. In *Proceedings of the IEEE/CVF conference on computer vision and pattern recognition*, pages 7922–7931, 2019. 3
- [75] Sijie Yan, Yuanjun Xiong, and Dahua Lin. Spatial temporal graph convolutional networks for skeleton-based action recognition. In *Thirty-second AAAI conference on artificial intelligence*, 2018. 3, 5, 7, 8
- [76] Yuan Yao, Chang Liu, Dezhao Luo, Yu Zhou, and Qixiang Ye. Video playback rate perception for self-supervised spatio-temporal representation learning. In *Proceedings of the IEEE/CVF conference on computer vision and pattern recognition*, pages 6548–6557, 2020. 2
- [77] Weiyu Zhang, Menglong Zhu, and Konstantinos G. Derpanis. From actemes to action: A strongly-supervised representation for detailed action understanding. In *2013 IEEE International Conference on Computer Vision*, pages 2248–2255, 2013. 5
- [78] Nenggan Zheng, Jun Wen, Risheng Liu, Liangqu Long, Jianhua Dai, and Zhefeng Gong. Unsupervised representation learning with long-term dynamics for skeleton based action recognition. In *Proceedings of the AAAI Conference on Artificial Intelligence*, volume 32, 2018. 2
- [79] Dingyuan Zhu, Ziwei Zhang, Peng Cui, and Wenwu Zhu. Robust graph convolutional networks against adversarial attacks. In *Proceedings of the 25th ACM SIGKDD international conference on knowledge discovery & data mining*, pages 1399–1407, 2019. 3
- [80] Will Y Zou, Andrew Y Ng, and Kai Yu. Unsupervised learning of visual invariance with temporal coherence. In *NIPS 2011 workshop on deep learning and unsupervised feature learning*, volume 3, 2011. 2